Chapter 2

Setup

From the experimental point of view we require time-resolution on the femtosecond scale, a vacuum chamber to house the apparatus necessary for electron spectroscopies on clean metal surfaces, and the means to determine the electron spin. These prerequisites determine our experimental setup, which has been designed, built up and characterised in the first two years of the thesis work.

2.1 Laser

The discovery of self mode-locking (or Kerr-lens mode-locking) in Ti:sapphire based lasers in 1991 initiated the commercial availability of reliable sources for ultrashort laser pulses [163, 29]. With such Ti:sapphire oscillators it is possible to generate laser pulses short enough to follow femtosecond (10^{-15} s) electron dynamics in a pump-probe experiment and with sufficient intensity for multiphoton excitation.
Extensive overviews regarding the physical phenomena encountered in ultrafast laser setups, such as spectral dispersion and compensation, intensity-dependent refraction, wavelength conversion and many more, can be found in [161, 61, 141, 146].
The laser system providing our ultrashort pulses is a home-built Kerr-lens mode-locked Ti:sapphire oscillator (cf. Fig. 2.1). In favour of tunability we decided on a prism-compensation scheme rather than dispersion compensation with chirped mirrors. The central wavelength of the laser pulses can be tuned from 850 to 725 nm with still acceptable output power of ≥ 400 mW at 5.2 W pump power. Our setup reliably produces stable, compressible ultrashort laser pulses between 25 fs and 45 fs pulse duration with a repetition rate of 88 MHz and an average output power of 920 mW around the peak

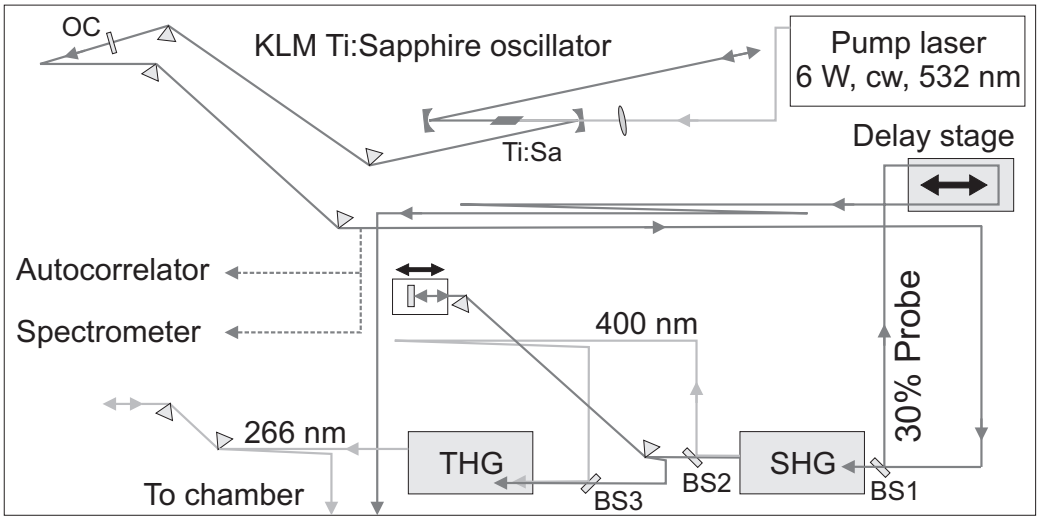

Figure 2.1: Schematic of the laser table with Kerr-lens mode-locked Ti:sapphire oscillator, delay path for the probe pulse, and second harmonic generation (SHG) with subsequent sum frequency generation of first and second harmonic, i.e. third harmonic generation (THG), for the pump pulse.

wavelength of 800 nm.

We thus can place emphasis on either a high time resolution (short pulses with a large bandwidth) or a better energy resolution in our photoemission experiment. For excitation of electrons into image-potential states we require photon energies on the order of the work function of our samples. Hence a major part of the output intensity is frequency-tripled via second harmonic generation (SHG) and subsequent sum-frequency generation (SFG) (schematically shown in Fig. 2.1). The third-harmonic pulse is used as a pump pulse in our photoemission experiment while the fundamental frequency supplies the probe pulse. A translation stage in the path of the probe beam controls the time-delay between pump and probe pulse.

With 70% of the oscillator output used for frequency conversion, we obtain intensities up to 19 mW at 266 nm for the pump pulse. Depending on the demands of the experiment, we can split off up to 50% for the IR probe beam and still achieve UV intensities of up to 5 mW.

In the following I describe in more detail the setup of our femtosecond light source with emphasis on new developments, which enabled us to improve the laser performance adequately for our spin-resolved two-photon photoemission experiment. As these details are not essential for the comprehension of the results, the reader primarily interested in the photoemission measurements may want to continue with Section 2.2.

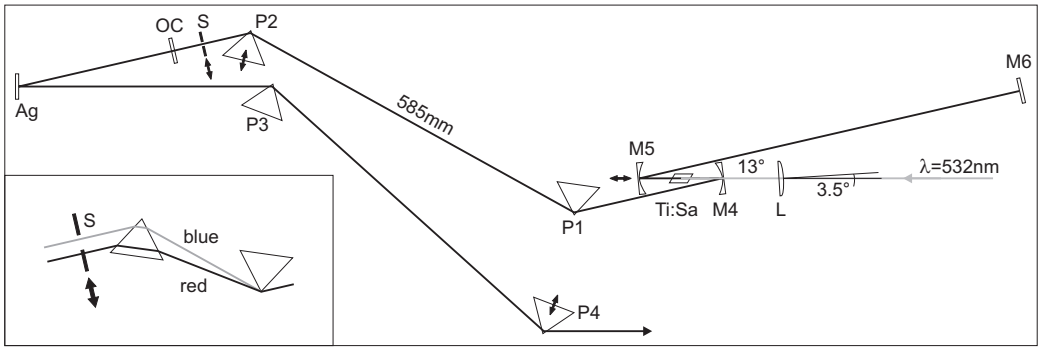

Figure 2.2: Schematic of the Kerr-lens mode-locked Ti:sapphire oscillator. The inset indicates the principle of wavelength tunability in our resonator.

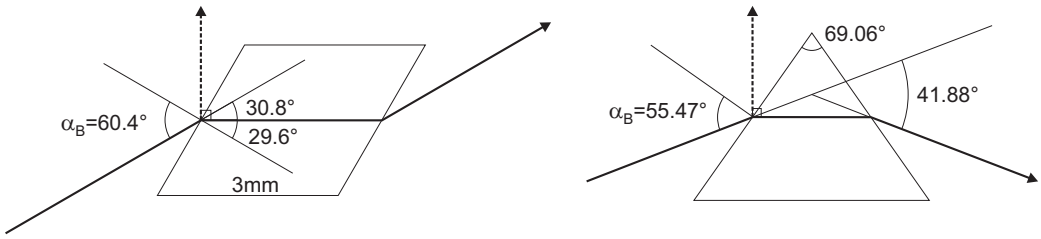

Figure 2.3: Left: Geometry of our 3 mm long Ti:sapphire crystal; the surface is Brewster-angle cut. Right: Geometry of our dispersion prisms. The apex angle is chosen such that a beam incident at the Brewster angle traverses the prism symmetrically (parallel to its base). Then the deviation is minimal and independent of the amount of glass between apex and beam path.

2.1.1 Details of the laser setup

Due to the diffraction at the tungsten crystal in the SPLEED detector (cf. Section 2.2), spin-resolved photoemission suffers from severe losses in count rate of up to four orders of magnitude in comparison with conventional photoemission. With bichromatic two-photon photoemission, a count rate of 10^5 counts/s in the $n = 1$ image-potential state on the clean Cu(100) surface is usually achieved [160]. In order to observe the electron dynamics in the image-potential states with spin resolution, higher count rates were necessary. Consequently we had to place great emphasis on an adequate output power of our oscillator while simultaneously avoiding direct photoemission and hence space charge effects due to abundant UV power.

Oscillator

The setup of our oscillator (shown in Fig. 2.2) closely resembles the Z-type scheme suggested in Reference [163]. The titanium doped sapphire[1] is pumped by a 6 Watt diode-pumped Nd:vanadate continuous wave (cw) laser, frequency-doubled to 532 nm (Coherent VERDI V6). A lens (L) is used to focus the pump laser beam onto the Ti:sapphire crystal. Two concave mirrors[2] (M4,M5) focus the laser radiation onto the Brewster-angle cut Ti:sapphire (cf. Fig. 2.3). Our sapphire crystal is comparatively small, which allows for extremely efficient water-cooling, successfully preventing the formation of a thermal lens. With a small angle between the surface normal of the lens and the incident beam, the overlap of the pump beam with the cavity mode can be improved [116, 5]. In combination with the folding angle (13°) of the cavity (as a function of the length of the Ti:sapphire crystal), the asymmetry of the arm-lengths (M5-M6 and M4-P1-P2-OC) and the position of the Ti:sapphire relative to M5, the astigmatism associated with the off-normal incidence on the curved mirrors M4,M5 is compensated and a symmetric Gaussian transverse mode can be acquired. Thus the detailed resonator configuration determines the stability and misalignment sensitivity of the oscillator [134, 33, 63, 178].
A pair of Brewster-cut fused-silica prisms (P1,P2) compensates the spectral dispersion introduced in the sapphire crystal [60, 7]. It should be noted here that femtosecond pulse generation requires a net negative dispersion in the cavity [99]. With the doping concentration in our Ti:sapphire crystal considerably increased[3], a significantly shorter crystal is sufficient for optimal pump power conversion. Additionally, the amount of dispersive media within the oscillator cavity is reduced and shorter pulses can be obtained [35]. A broad-band high reflecting mirror (M6) and an output coupler (OC) with 12% transmission complete the cavity. Because the pulse is coupled out at the dispersed end of the cavity, a matching extracavity prism pair (P3,P4) is required, which can additionally compensate the dispersion picked up in the output coupler.
In principle, the refractive index of any medium is a function of incident

[1] With an ultrabroad gain bandwidth from 700 to 1100 nm, high-gain cross-section, large damage threshold and high thermal conductivity, the extremely polar material titanium-doped Al_2O_3 (Ti:sapphire) is predestined as gain medium for ultrashort laser pulses [114].

[2] These broad-band mirrors are usually employed in the Coherent MIRA 900 tunable oscillator.

[3] Absorption coefficient $\alpha(532\text{nm}) = 5\ \text{cm}^{-1}$ at the pump laser wavelength of 532 nm

intensity

$$n(I) = n_0 + n_2(I) \ , \tag{2.1}$$

but the nonlinear refractive index n_2 is very small and usually negligible. However, for the ultrahigh intensities encountered in an ultrashort laser pulse this optical Kerr effect [133] can lead to self-focusing of the laser beam in the Ti:sapphire. To stabilise the mode-locked state in an oscillator, the curved mirrors M4,M5 are not confocal in the sense of linear optics. Only in combination with the Kerr lens in the Ti:sapphire is the cavity perfectly aligned. The distance M4-M5 is therefore crucial to determine the stability region (cw or mode-locked) of the cavity. Mode-locking is initiated in our oscillator by tapping prism P2 and thereby introducing a small intensity fluctuation, which becomes the seed of a pulse.
With a movable slit (S) between P2 and the output coupler, where the pulse is spectrally spread out in space, the central wavelength of the laser pulses can be tuned from 850 to 725 nm with still acceptable output power of $\geq$ 400 mW. The amount of dispersive material in the cavity, i.e. the total dispersion and with this the pulse length can be varied by inserting prism P2 further into the beam path. In combination with the slit position, our setup reliably produces stable compressible ultra short laser pulses between 25 fs and 45 fs with a repetition rate of 88 MHz and an average output power of 920 mW at 5.2 W pump power from the Nd:vanadate laser.

Wavelength conversion

The majority of the output intensity (50-90%) is required for the generation of frequency-tripled pulses. The second harmonic is generated in a 1 mm long lithium triborate (LBO) crystal with type I (critical) phase matching[4]. As higher harmonic generation is a nonlinear effect, a high intensity in the LBO is desired for efficient conversion. The beam diameter in the focal plane of the cavity for second harmonic generation (SHG) can be minimised by increasing the incident beam diameter. As the beam emerging from the oscillator is slightly divergent, we simply increased the distance between the oscillator and the SHG cavity, thereby gaining approximately 5% intensity in the second harmonic. A further increase in conversion efficiency by 25% was

[4]In a birefringent crystal such as BBO or LBO the refractive index is anisotropic and depends on the angle between polarisation vector and optical axis. With the polarisation $\mathbf{P}_\omega$ of the fundamental frequency perpendicular to the polarisation of the second harmonic $\mathbf{P}_{2\omega}$, the optical axis $\mathbf{O}$ can be oriented such that always $\mathbf{P}_\omega \perp \mathbf{O}$. Then the phase velocity for fundamental and second harmonic can be matched by rotating the crystal and varying $\angle(\mathbf{O}, \mathbf{P}_{2\omega})$ [146].

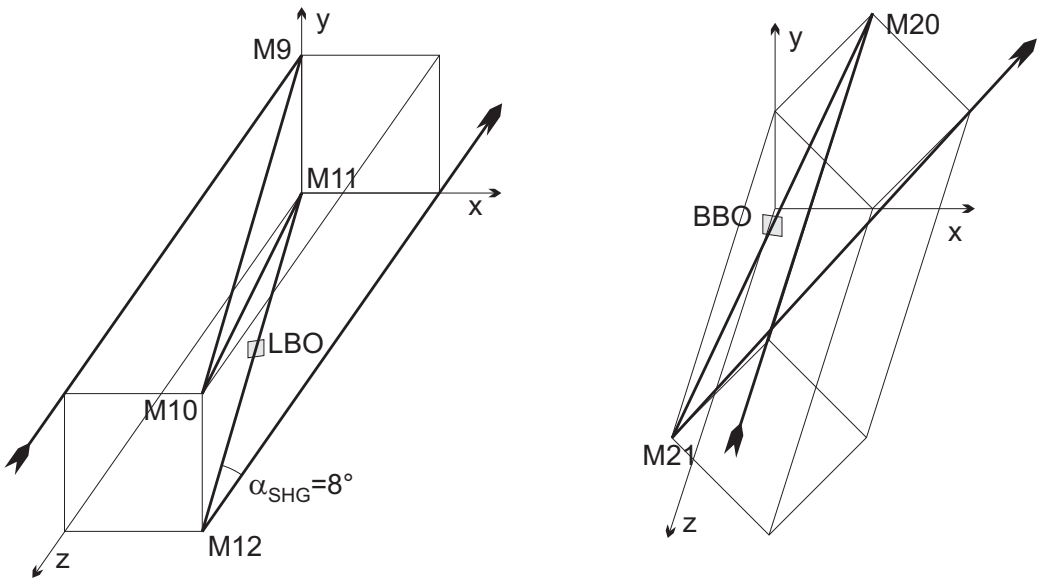

Figure 2.4: Left: Schematic of the beam path in the SHG cavity. A small folding angle α_{SHG} minimises astigmatism. For a perfectly recollimated beam after M12 the tangential plane for reflection at M11 must coincide with the sagittal plane for reflection at M12 and vice versa [72]. Right: Beam path in the THG cavity. With the 45° tilted design the beam exits the cavity parallel to the laser table.

observed after reducing the folding angle of the SHG cavity (cf. Fig. 2.4) from 10° to 8°, moderating the effect of astigmatism introduced by the non-normal incidence on the curved mirrors. Here the limiting factor is the mounting of the LBO crystal, which grazes the beam at small angles.
Due to the large tunable range of our oscillator, the polarisation of the second harmonic after the LBO crystal is rotated back to horizontal by a periscope rather than a $\lambda/2$ plate. The remaining infrared light is recompressed and the relative time delay between fundamental and second harmonic is adjusted. Additional recompression of the second harmonic after SHG with a prism pair could not increase the intensity of the third harmonic for the pulse lengths we generally use in the experiment.
The third harmonic is generated by sum frequency generation in a 100 μm long β-barium borate (BBO) crystal, also with type I phase matching. Steering mirrors with an incidence angle other than 0° or 45° must be metal mirrors, which have a much lower reflectivity than dielectric mirrors. Hence we reduced the number of metal mirrors with a 45° rotated THG (third harmonic generation) cavity, such that the incident beam as well as the outgoing beam are both parallel to the laser table (as shown in Fig. 2.4).
It is essential for the two-photon photoemission experiment to adjust the beam diameter of the UV pulse (with the collimating mirror in the THG cavity) such that the spot diameter of the focussed UV pump and IR probe beam eventually coincide on the sample. After the THG cavity, the polarisation of the UV pulse is rotated in plane and the dispersion compensated in a prism-pair compressor.

Pulse characterisation

The time-bandwidth product $\Delta\nu \cdot \Delta\tau_p = 0.4413$ for a Gaussian pulse shape belongs to the shortest pulse width $\Delta\tau_p$ obtainable from a given spectral width $\Delta\nu$. With the measurement of an interferometric autocorrelation, it can be determined whether the pulse is indeed as short as possible [42, 117]. In an interferometer the pulse is split and the two halves are overlapped in a nonlinear crystal such as BBO. The second harmonic intensity as a function of relative time delay τ is then given by

$$I_{2\omega} = \int |[\mathcal{E}(t) + \mathcal{E}(t-\tau)]^2|^2 dt \ , \tag{2.2}$$

where $\mathcal{E}(t)$ is the electric field of the laser pulse. An interferometric autocorrelation yields a peak-to-background ratio of 8 : 1, though it requires careful alignment of the beam to reach this ratio in the experiment. Deviations

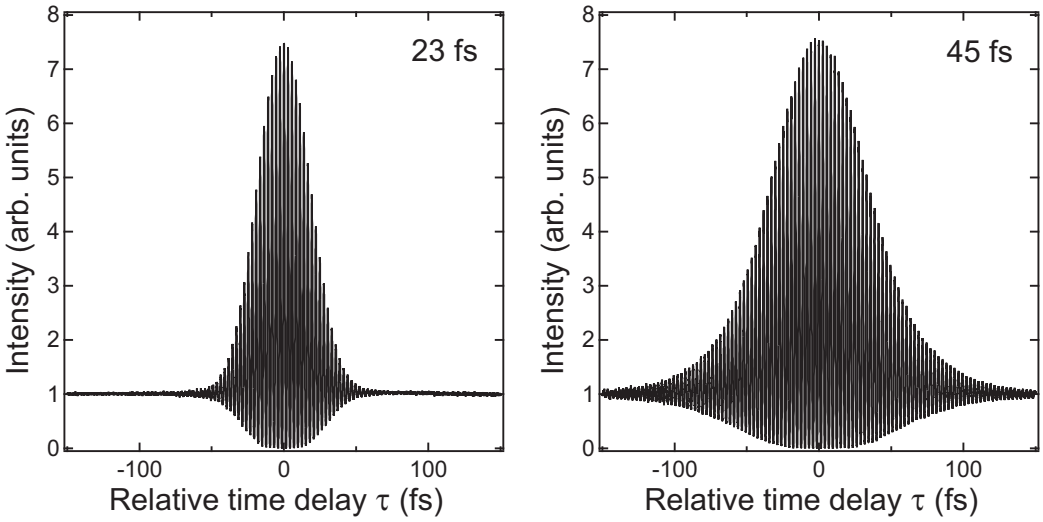

Figure 2.5: Two examples of interferometric autocorrelations of pulses with a central wavelength of 795 nm obtained from our oscillator. The pulse lengths are 23 fs and 45 fs.

of the pulse from its bandwidth-limited duration, like a chirp for example, i.e. a delay between the spectral components of the pulse, can be indicated by changes in the form of the autocorrelation. For the characterisation of the pulses from our oscillator we usually recorded a spectrum as well as the fringe-resolved autocorrelation. Figure 2.5 shows two examples of interferometric autocorrelations obtained from our oscillator. The panel on the left contains the autocorrelation of a pulse optimised for low pulse duration, and the autocorrelation of a longer pulse suited for higher energy resolution in the photoemission measurement can be seen in the right panel.

2.2 Chamber

For surface analysis techniques like photoemission spectroscopy an ultrahigh vacuum (UHV) is required to prevent contamination of the surface through adsorption of residual gas molecules. At a base pressure of $1 \cdot 10^{-10}$ mbar a surface is usually covered with one monolayer of residual gas molecules after a couple of hours [73]. As surface states are particularly sensitive to adsorbates special care must be taken to avoid contamination during the measurements. Our UHV chamber consists of three parts, preparation, analysis and spin detection, each equipped individually with an ion getter pump and titanium sublimation pump in addition to the typical combination of rotary vane pump and turbomolecular pump. The preparation chamber can be sealed off from

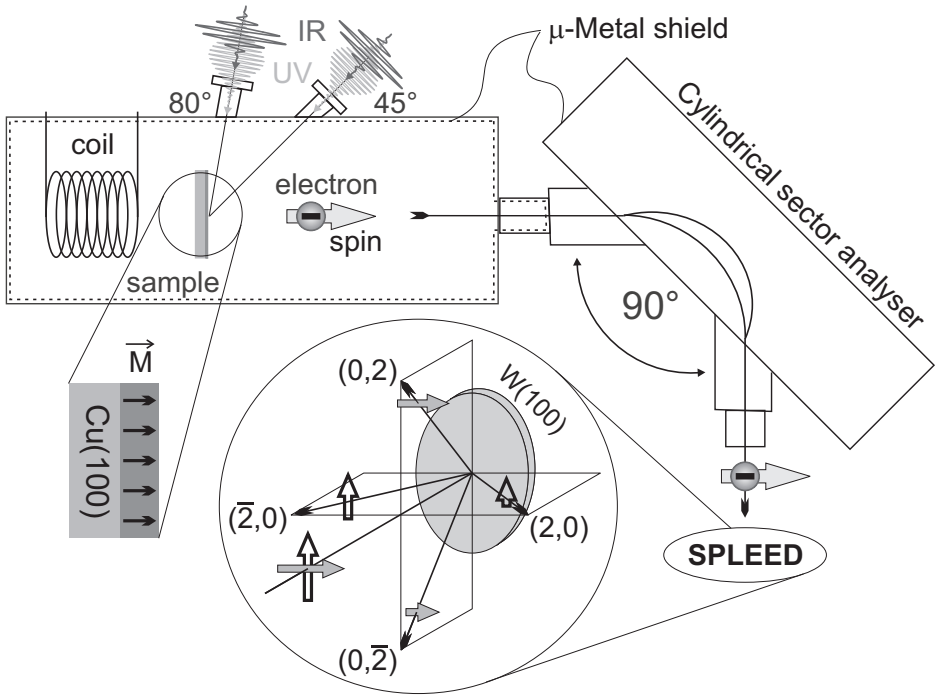

Figure 2.6: Schematic of the UHV chamber in the analysis plane.

the analysis and spin-detection chambers with a plate valve, effectively preventing contamination of these chambers during sample preparation. The preparation chamber houses an ion gun for argon ion sputtering of the samples, a (retractable) low-energy electron diffraction (LEED) gun and optics for surface structure analysis, a medium-energy electron diffraction (MEED) gun for real-time monitoring of thin film growth (using the phosphor screen of the LEED optics as detection device), an evaporator for iron and cobalt and a water-cooled quartz microbalance for calibration of the evaporators.
A Cu(100) and a Cu(111) single crystal are used as substrates for the magnetic films. They are mounted on a rotatable 3-axis manipulator for correct positioning of the samples for e.g. evaporation or in the focus of the electron analyser. The hollow arm of the manipulator can be used as coolant reservoir for either water or liquid nitrogen. A copper block at the lower end provides thermal conductivity between the samples and the reservoir. Resistive heating is employed for the Cu(111) crystal, while the Cu(100) crystal can be heated through radiant heating and electron bombardment from tungsten filaments. The two tungsten coils are attached antiparallel to the manipulator in order to minimise stray magnetic fields. A Type E thermocouple is employed as temperature sensor on both samples. The Type E Chromel (Ni-Cr alloy) – Constantan (Cu-Ni alloy) thermocouple is non-magnetic and

has a comparatively high output voltage per K down to liquid nitrogen temperatures.
Below the preparation chamber, the analysis plane, as shown in Figure 2.6, comprises the analysis chamber, the electron energy analyser and the spin detection. Two fused silica entrance windows permit an angle of incidence for the laser pulses of 45° or 80° with respect to the surface normal. A rotatable coil is used to remanently magnetise the thin ferromagnetic films either in-plane (with the coil below the sample) or perpendicular to the surface (with the coil behind the sample), according to the respective easy axis of magnetisation. The μ-metal shielding of the electron energy analyser housing is extended to cover the entire analysis chamber, suppressing the earth's magnetic field to below 2 mG.
Electrons emitted from the sample propagate towards the energy analyser, where they are accelerated or decelerated, depending on their kinetic energy, to the pass energy of typically 1 eV. The energy analyser is a 300 mm, 90° cylindrical sector analyser (Focus GmbH). The energy resolution can be estimated from the width of the low-energy cut-off in photoemission spectra (cf. Section 3.3) [156]. In our usual configuration with the 6 mm entrance slit and the 3 mm exit split, the energy resolution of the analyser amounts to 65 meV. An aperture in front of the electron optics ensures an angular resolution of ±2.5°.
The spin polarisation P of the electrons is determined in the SPLEED (spin-polarised low energy electron diffraction) detector [89]. Spin-orbit coupling in the high-Z element tungsten leads to a polarisation-dependent asymmetry

$$A = \frac{I_1 - I_2}{I_1 + I_2} = SP \tag{2.3}$$

in the intensity I_1, I_2 of the diffracted beams (schematically represented by the length of the arrows in the inset of Figure 2.6). With four channeltrons placed in the corresponding diffraction spots, the detector is polarisation-sensitive in two perpendicular scattering planes (solid and open arrows). Unfortunately up to four orders of magnitude in intensity are lost in the diffraction process.
The Sherman function S, which corresponds to the asymmetry of a 100% spin-polarised beam ($P = 1$), is a measure of the sensitivity of the detector. Though it is difficult to determine, a number of measurements can be used for a rough calibration [135]. Especially photoemission peaks with a strong spin polarisation tend to yield unphysical results with a wrong value for the Sherman function. The theoretically predicted value of $S_{\mathrm{th}} = 0.33$ constitutes an upper limit for S [89]. In our setup a Sherman function of $S \leq 0.22$

amounts to negative intensities in the minority-spin channel for a strongly spin-polarised electron beam. Throughout this work a Sherman function of $S = 0.24$ is assumed. Note that a systematic error introduced by this choice is not included in the error bars.
Instrumental asymmetries cancel if the experiment is repeated with the direction of magnetisation reversed. The spin polarisation is then obtained from the geometrical mean of the two measurements

$$P = \frac{1}{S}\frac{\sqrt{I_1 I_2'} - \sqrt{I_2 I_1'}}{\sqrt{I_1 I_2'} + \sqrt{I_2 I_1'}} , \tag{2.4}$$

with $'$ indicating the second measurement with reversed magnetisation [87].

2.3 Samples

We have investigated ultrathin iron and cobalt films grown epitaxially on a Cu(100) single crystal substrate.
The Cu(100) single crystal surface was prepared by cycles of sputtering with 800 eV Ar^+ ions and subsequent annealing to 560°C temperature. The films were grown by evaporation of cobalt or iron from a rod heated by electron bombardment[5].
The interest in iron films grown on copper sparked in the hope of stabilising ferromagnetic face-centred cubic (fcc) iron at room temperature[6]. Due to their uniquely complex structural behaviour and its correlation to the magnetic properties that interest never completely abated during the last decades [173, 115, 18, 19, 164, 13, 82]. After a wealth of experimental and theoretical studies a consensus has been reached that the magnetic property of iron deposited on Cu(100) at room temperature runs through three different coverage regimes. Up to about 4 ML (regime I) the Fe film is ferromagnetic throughout with the easy axis of magnetisation perpendicular to the film plane. The easy axis is still perpendicular to the surface between 5 and 10 ML (regime II), but only the top three layers are ferromagnetically coupled while the layers below show antiferromagnetic ordering. It has also been suggested that the magnetic structure of the underlying fcc Fe on Cu(100) in regime II may be a spin-density wave [139]. At still higher coverage (regime

[5]Homebuilt electron beam evaporator equivalent to Omicron's EFM 3

[6]Bulk iron undergoes a structural phase transition at 1183 K from bcc (α-Fe) to fcc (γ-Fe) and a magnetic phase transition from ferromagnetic to paramagnetic at $T_C = 1044$ K. The lattice constant $a = 3.65$ Å of γ-Fe is remarkably close to the lattice constant of Cu at room temperature with $a = 3.61$ Å [106]

III) the film becomes ferromagnetic body-centred cubic (bcc) iron with an in-plane magnetisation direction (along the Cu[100] direction). The coverage regime up to 10 ML shows indeed an fcc-like ferromagnetic structure though there is an ongoing discussion whether the crystal structure in regime I is bcc rather than shear-deformed fcc. Only recently did investigations with ion beam triangulation yield strong evidence in favour of the fcc structure, with a possible exception of 3 ML iron, where the structure seems more distorted than at other coverages [13].
This is consistent with MEED traces recorded during the growth of iron on Cu(100) [173]. After the first bilayer, iron exhibits layer-by-layer growth, which can be followed with MEED up to the transition from regime II to regime III. While the second and fourth layer show strong MEED reflectivity, the 3 ML peak is slightly smaller.
Nevertheless we investigated mainly 3 ML Fe/Cu(100). The Curie temperature of thin ferromagnetic films is much smaller than for the bulk ferromagnets, often close to room temperature [41]. In order to observe the full exchange splitting, measurements were mainly carried out at a temperature of 90 K. As a reversal of the magnetisation direction rids us of experimental asymmetries, we require films with a coercive field smaller than our coil can provide. We were always able to reverse the magnetisation direction of the 3 ML films quite easily, while especially for 2 and 4 ML films we had to resort to heating of the sample, thereby lowering the coercitivity. Obviously the slight distortion of the 3 ML film lowers its coercitivity compared to 2 and 4 ML.
Of course we investigated also 2 and 4 ML iron, but found almost no deviations in terms of electron dynamics. In the instances where differences were observed, both results will be shown.
Our iron films were grown at room temperature (low-temperature grown iron has different structural and magnetic properties), where the coverage could be monitored with MEED during the growth process. Annealing of the Fe films is not possible as it creates pinholes in the films already at mild annealing temperatures [158]. After evaporation the samples were cooled to liquid nitrogen temperature, where the measurements were carried out.
Though the native crystal structure of cobalt at room temperature is hexagonally close-packed (hcp), the lattice constant $a = 3.55$ Å of the high temperature phase of bulk Co is also close to that of Cu[7] [106]. Indeed, Co films exhibit pseudomorphic growth on Cu(100) in an fcc structure with the easy

[7]The structural phase transition from hcp (ε-Co) to fcc (α-Co) Co occurs at $T = 661$ K. Bulk Co has a Curie temperature of 1388 K.

axis of magnetisation in the film plane along the Cu[110] direction [150, 54]. The peril in growing cobalt films on copper lies in intermixing and Cu segregation, which is already significant at room temperature and can become strong for low evaporation rates [81, 14]. We therefore grow the cobalt films at 90 K (after carefully calibrating the evaporation rate), where Co grows first in a bilayer followed by layer-by-layer mode and no intermixing occurs. Additionally, a smooth surface is required as the image-potential states are extremely sensitive on the surface morphology. Without annealing no image-potential state can be detected on low-temperature grown films.

Density-functional theory studies of the growth process of Co on Cu suggest that eventually the energetically preferred structure is a single Cu capping layer on top of the Co film. During the evaporation of Co on the Cu substrate, Cu segregates onto the surface via Co/Cu exchange processes. These processes occur already at room temperature during the evaporation, providing "stepping stones" for the Cu atoms on their way to the topmost layer. With increasing film thickness substitutional adsorption of Co becomes less likely [119, 129, 130].

Due to the immiscibility of Co and Cu in the bulk phase [3], we estimated that intermixing and diffusion of Cu atoms on top of the surface might be avoided even at elevated temperatures if these initial interchange processes are prevented. Measurements of quantum-well states, which are strongly sensitive to interface roughness, support the assumption that in low-temperature grown Co films on Cu(100) no initial intermixing occurs [187, 121, 166]. We therefore grew our Co films at 90 K to produce a sharp interface between Co and Cu, subsequently annealing the film to also achieve a smooth surface.

In a series of experiments with low-temperature grown films subsequently annealed to increasingly higher temperatures, we found that an annealing temperature of 210°C yields photoemission spectra with intense but narrow image-potential peaks (the measurements were always carried out with liquid nitrogen cooling at 90 K). Films annealed to 250°C or higher show a reduced exchange splitting of the first image-potential state, slightly increased linewidths and less intensity. We interpret this in terms of an onset of Cu segregation to the surface at 250°C. An inhomogeneous Co/Cu alloy at the surface with a consequently smaller magnetic moment might be the cause of the increased linewidths and the reduced exchange splitting.

Further conclusions drawn from the time- and spin-resolved two-photon photoemission data acquired during these preparation tests will be analysed in Section 4.5.

All measurements shown in this work will be confined to 6 monolayer cobalt

on copper (6 ML Co/Cu(100)) and 3 ML Fe/Cu(100), with a few exceptions where iron is concerned.